Response of shock interaction patterns to different freestream conditions in carbon-dioxide flows over double-wedges

Catarina Garbacz * and Fábio Morgado † and Marco Fossati ‡
Aerospace Centre, University of Strathclyde, Glasgow, G1 1XJ, United Kingdom

The shock interaction originating from a hypersonic laminar flow over a double-wedge can lead to different flow patterns depending on geometrical parameters such as the lengths and angles of the each wedge, as well as flow parameters such as the mixture and freestream conditions. In this work, the effect of the freestream Mach number on the patterns of shock interaction is numerically investigated for a CO_2-N_2 nonequilibrium flow over different double-wedge geometries. The numerical analysis is performed by solving the laminar Navier–Stokes equations within the framework of a two-temperature model to account for translational–vibrational internal energy transfer. Results show that the size of separated flow regions, both in the compression corner and locations of shock impingement, increase with decreasing Mach number. This revealed to have a significant impact on the patterns of interaction, since the size of a separation region dictates if additional shocks are generated, potentially leading to more complex mechanisms of interaction. It was concluded that decreasing the freestream Mach number has a similar impact as increasing the angle of the second wedge on the pattern of interaction. The parametric study also shows that decreasing the freestream Mach number leads to overall lower surface pressure and heating, as well as smaller regions of thermal equilibrium.

I. Introduction

In hypersonic flight, shock waves originating at different parts of the vehicle may interact and lead to complex flow physics. Depending on the patterns of interaction, flow separation and reattachment, as well as shock wave impingement, may occur, resulting in extremely high and localised peaks of pressure and heating on the surface. From the viewpoint of aerodynamic design, it is imperative to ensure that the vehicle can withstand its aerothermodynamic environment and this is only possible by accurately estimating the distribution of surface aerothermal loads resulting from given flow patterns. The most cost-effective and accessible approach to tackling this problem is computational fluid dynamics, but detailed models are required to account for underlying physical processes in the numerical prediction. In particular, when the hypersonic flow is rapidly decelerated across a shock wave, vibrational modes of molecules are excited and chemical reactions take place. At high freestream velocities, the relaxation times of these finite-rate processes are of the order of the fluid mechanical residence time and the flow may be in thermochemical nonequilibrium. Several studies have shown that the presence of nonequilibrium effects can greatly influence the structure of the shock wave system and associated surface loads [1–3].

The canonical double-wedge geometry is very useful for investigating the detailed physics involved in Shock Shock Interactions (SSIs) and Shock Wave Boundary Layer Interactions (SWBLIs), as it represents the generic shape of deflected aerodynamics control surfaces or two-dimensional hypersonic intakes. The interaction between a shock formed by the fuselage and the shock generated at the wing of a vehicle can also be modelled as double-wedge. The type of interaction that occurs depends on specific non-dimensional parameters, which for inviscid flow and calorically perfect gas are the Mach number M, the ratio of specific heats γ, the ratio of the first wedge face length to the second wedge face length L_2/L_1, and the two wedge angles θ_1 and θ_2 [4]. In the case of viscous flow, the Reynolds number Re will also influence the pattern of interaction. When high-temperature effects such as finite-rate chemistry and thermal nonequilibrium are present, the freestream temperature is an additional critical parameter, since it has a significant impact on nonequilibrium processes. In the latter case, the mixture, rather than the specific heat ratio, would be used to characterise the gas dynamics.

The effect of the geometry on shock interaction patterns has been extensively studied in the literature [4–8]. Exploring the changes in the flow as a result of increasing the angle of the second wedge has revealed that the separated

*PhD student, Department Mechanical and Aerospace Engineering, AIAA Member.
†PhD student, Department Mechanical and Aerospace Engineering, AIAA Member.
‡Associate Professor, Department Mechanical and Aerospace Engineering, AIAA Member.

This is a peer reviewed, accepted author manuscript of the following research paper: Garbacz, C., Morgado, F., & Fossati, M. (2022). Response of shock interaction patterns to different freestream conditions in carbon-dioxide flows over double-wedges. In AIAA AVIATION 2022 Forum [2022-3277] (AIAA AVIATION 2022 Forum). American Institute of Aeronautics and Astronautics Inc, AIAA. https://doi.org/10.2514/6.2022-3277

region generated by the compression corner continuously thickens, and the separation point moves toward the leading edge [8]. Additionally, larger aft angles lead to a larger standoff distance of the bow shock, higher probability of shock impingement on the wall and overall increasing complexity of the interaction mechanism, potentially leading to instability of the shear layers or unsteady interaction patterns [5, 8]. Efforts have also been made in the attempt to better understand the influence of the gas mixture and/or specific heat ratio on the physics of shock interactions [9, 10]. Tumuklu et al. compared the flow over a 30°-55°double-wedge for three different gas mixtures: air, nitrogen, and argon [9]. The size of the separation region, the upstream movement of the triple-point, and the time for the flow to reach steady state revealed to be much less for air than for the case of nitrogen. The flow of argon exhibited the fastest movement of the triple-point relative to the other two mixtures. In Ref. [10], the role of the gas mixture was further investigated. It was concluded that the relative magnitude of the specific heat ratio has a significant impact on SBLI (Shock Boundary Layer Interaction). Specifically, the flow of argon resulted in a separation bubble with 1.8 times the size of the one for nitrogen and—due to the endothermic effects of finite-rate chemistry— the size of this region was 1.5 smaller for air than for nitrogen. In hypersonic shock interactions where nonequilibrium effects play a? role, the freestream temperature has been shown to have a significant impact on the flow patterns [6, 11]. The authors of this paper conducted previous numerical studies simulating the flow over a double-wedge, for different gas mixtures and freestream temperatures, T_∞ = 300 K and T_∞ = 1000 K [11]. Results showed a great change in the shock wave pattern for the case of an air mixture, whereas for the CO_2–N_2 case the change of pattern did not occur. This was attributed to the much faster vibrational relaxation of CO_2 molecules, as the flows with a CO_2–N_2 mixture revealed overall much smaller discrepancies between translational and vibrational temperature. Similar conclusions concerning the flow of air were drawn in Ref. [6]. Further, the influence of the freestream Mach number has been assessed in Refs. [6, 12]. A computational analysis of a flow of air over a double-wedge, with M_∞ = 7.14 and M_∞ = 7.3, revealed that increasing the freestream Mach number results in later flow separation and larger values of the heat flux peaks at reattachment and impinging shock regions, despite presenting the same qualitative distribution of the surface quantities [12]. In Ref. [6], the freestream Mach number was increased from 2.8 to 9. The resulting flow field was significantly affected, with the larger value of Mach number leading to reduced shock angles, increased real gas effects that further contribute to smaller shock standoff distances and a significant rise in pressure.

Despite continued research effort on the topic of shock interference when it comes to flows of air or nitrogen [1, 3–5, 7, 13–15], the literature pertaining other gas mixtures is still scarce to the best of the authors' knowledge [9, 16]. These works draws specific attention to CO_2-dominated mixtures, which have become relevant in the aerospace scientific community due to recent Mars exploration programs. The internal structure of the CO_2 polyatomic molecule is different from the diatomic molecules of air, which affects the process of energy redistribution amongst the different internal modes and, in turn, the macroscopic properties of the flow. Previous work conducted by the authors of this paper compared inviscid flow over a double-wedge geometry for mixtures of air and CO_2, using the two-temperature model by Park [17]. Results have confirmed that the different molecular structures and behaviour of nonequilibrium finite-rate processes have a significant impact on the obtained shock interaction patterns and associated surface loads. To better understand nonequilibrium shock interaction physics in CO2-dominated flows, the authors recently investigated the impact of increasing the aft wedge angle as well as the impact of using different thermo-physical models for the mixture, comparing the flow patterns obtained with Park's two-temperature model to those obtained with thermally perfect and perfect ideal gas models. Increasing the aft angle significantly enlarged the separated region in the compression corner, generating numerous secondary shock waves and shear layers. Except for the case of the maximum angle, when the strongest peaks were owing to shock impingement, heat flux and pressure peaks with increasing intensity occurred along the surface due to boundary layer reattachment downstream of the compression corner. The size of the recirculation bubble at the compression corner, the shock interaction mechanism and the surface loads were all shown to be heavily influenced by the different assumptions on vibrational mode excitation. When a larger portion of the internal energy is absorbed by the vibrational mode, lower post-shock temperatures are obtained, which tends to increase post-shock density, resulting in weaker shock interactions characterised by delayed onsets of separation, reduced separation regions, and smaller standoff distance.

After investigating the effect of freestream temperature, geometry and physical model on the nonequilibrium CO_2 flow over the double-wedge, this work proposes to investigate the response of the hypersonic shock wave system to different values of Mach number in the freestream flow. Numerical simulations are performed for a viscous flow over two different double-wedge geometries (15°-45°and 15°-55°) and three different values of the freestream Mach number (7, 9 and 11). The SU2-NEMO [18] solver is used together with the Mutation++ library [19], considering the Park's two-temperature model to address nonequilibrium in the flow. This paper is organized as follows: Section II introduces the governing equations and physical models. Section III gives an overview of the solvers and numerical models.

Section IV presents the double-wedge geometry together with the computational domain and boundary conditions, and additionally introduces some of the generic flow physics and patterns to be discussed in the computational analysis. Section V shows the grid convergence study and presents the parametric study of the nonequilibrium shock interaction mechanisms with respect to the freestream Mach number. In Section VI, the main conclusions are summarized.

II. Physical Modelling

The system of governing equations implemented with the nonequilibrium models follows the Navier-Stokes approach presented in the literature for a continuum, viscous laminar, chemically-reacting, thermal nonequilibrium flow [20]. The two-temperature model by Park is used to model thermal nonequilibrium. It has been developed initially for air [17] but later modified for CO_2 flows [21] and validated in refs. [22, 23] against experimental data and the more detailed state-to-state approach. The model assumes that rotational relaxation is very fast relative to the rate of fluid motion and therefore considers that the translational and rotational modes of the gas are in equilibrium with each other at the translational-rotational temperature T_{tr}. As for vibrational relaxation, the CO_2 triatomic molecule has three vibrational modes, one of which is double degenerate. Camac [24] showed that all three modes relax at the same time, but considerably slower than the rate of fluid motion, leading to a single separate temperature to describe this process. Electronic modes are assumed to be at equilibrium with vibration, therefore it is considered that these two modes relax at the vibro-electronic temperature T_{ve}. In a compact form, the system of equations can be described as

$$\frac{\mathrm{d}\mathbf{U}}{\mathrm{d}t} + \nabla \cdot \vec{\mathbf{F}}^{\text{c}}(\mathbf{U}) = \nabla \cdot \vec{\mathbf{F}}^{\text{v}}(\mathbf{U}) + \mathbf{Q}(\mathbf{U}) \tag{1}$$

where the conservative variables, convective fluxes, viscous fluxes, and source terms are given by

$$\mathbf{U} = \begin{Bmatrix} \rho_1 \\ \dots \\ \rho_{n_s} \\ \rho\vec{u} \\ \rho e \\ \rho e^{\text{ve}} \end{Bmatrix}, \quad \vec{\mathbf{F}}^{\text{c}} = \begin{Bmatrix} \rho_1\vec{u} \\ \dots \\ \rho_{n_s}\vec{u} \\ \rho\vec{u}\otimes\vec{u} + p\bar{I} \\ \rho h\vec{u} \\ \rho e^{\text{ve}}\vec{u} \end{Bmatrix}, \quad \vec{\mathbf{F}}^{\text{v}} = \begin{Bmatrix} \vec{J}_1 \\ \dots \\ \vec{J}_{n_s} \\ \bar{\tau} \\ \bar{\tau}\cdot\vec{u} + \sum_s \vec{J}_s h_s + \vec{q}^{\text{ve}} + \vec{q}^{\text{tr}} \\ \sum_s \vec{J}_s h_s^{\text{ve}} + \vec{q}^{\text{ve}} \end{Bmatrix}, \quad \mathbf{Q} = \begin{Bmatrix} \dot{\omega}_1 \\ \dots \\ \dot{\omega}_{n_s} \\ 0 \\ 0 \\ \dot{\Omega} \end{Bmatrix} \tag{2}$$

and ρ is the density of the mixture, ρ_s is the partial density of species s, p is the static pressure, e and e^{ve} are, respectively, the total energy per unit mass and the vibrational energy per unit mass for the mixture, h is the total enthalpy per unit mass, $\vec{J}_s$ is the species mass diffusion flux, $\bar{\tau}$ is the viscous stress tensor, $\vec{q}$ is the conduction heat flux, index s denotes the s^{th} chemical species and n_s is the total number of species.

Calculating the nonequilibrium thermodynamic state and source terms is necessary to close the system of governing equations that describes hypersonic flows. This is achieved by means of coupling with appropriate multi-temperature thermochemistry models. The equations presented below describe the implementation of the two-temperature model for a mixture composed of neutral species, provided by the Mutation++ library [19]. Each individual species s is assumed to behave as an ideal gas. Hence, the total pressure of the mixture p is defined by Dalton's Law as the summation of the partial pressures associated with each species p_s, determined by the ideal gas law,

$$p = \sum_{s=1}^{n_s} p_s = \sum_{s=1}^{n_s} \rho_s \frac{R_{\text{u}}}{M_s} T_{\text{tr}}, \tag{3}$$

where R_{u} is the universal gas constant, M_s is the molar mass of species s and T_{tr} is the trans-rotational temperature. The total specific energy of the flow e is given as the sum of the internal and kinetic energies:

$$e = \sum_{s=1}^{n_s} c_s e_s + \frac{1}{2}u^2, \tag{4}$$

where c_s is the mass fraction of species s, u is the magnitude of the flow velocity vector and e_s is the specific internal energy of the species, given by the sum of the energy of formation and the contribution of each internal mode (t-translational, r-rotational, v-vibrational, e-electronic),

$$e_s = e_s^{\text{t}}(T_{\text{tr}}) + e_s^{\text{r}}(T_{\text{tr}}) + e_s^{\text{v}}(T_{\text{ve}}) + e_s^{\text{e}}(T_{\text{ve}}) + e_s^0. \tag{5}$$

In the two-temperature model, the energy transfer mechanisms, that determine the change in vibrational energy of the mixture, are accounted for in the source term vector. The source term $\dot{\Omega}$ is defined as the sum of the vibrational-to-translational energy transfer and energy exchanges due to chemical activity,

$$\dot{\Omega} = \sum_{s=1}^{n_s} \dot{\Omega}_s^{\text{tr:ve}} + \dot{\Omega}_s^{\text{c:v}} + \dot{\Omega}_s^{\text{c:e}}. \tag{6}$$

The term $\dot{\Omega}^{\text{tr:ve}}$ concerns the rate of energy exchange between the translational and vibrational energy modes, following the Landau-Teller model [25]

$$\dot{\Omega}_s^{\text{tr:ve}} = \rho_s \frac{e_s^{\text{v}}(T) - e_s^{\text{v}}(T_{\text{v}})}{\tau_s^{\text{V-T}}}. \tag{7}$$

The vibrational relaxation time of each species, $\tau_s^{\text{V-T}}$, is given by the Millikan and White empirical formula [26] and the Park correction [27]. The change in vibrational-electronic energy of the mixture due to the production/destruction of species is accounted for in the terms $\dot{\Omega}_s^{\text{c:v}}$ and $\dot{\Omega}_s^{\text{c:e}}$, given by

$$\dot{\Omega}_s^{\text{c:v}} = c_1 \dot{\omega}_s e_s^{\text{v}}, \qquad \dot{\Omega}_s^{\text{c:e}} = \dot{\omega}_s e_s^{\text{e}}. \tag{8}$$

A non-preferential dissociation model is considered to account for the coupling between vibrational energy modes and finite-rate chemistry. The model assumes that molecules are destroyed or created at the average vibrational energy of the cell, $c_1 = 1$.

III. Numerical Methods

The governing equations introduced in the previous section are numerically solved with the open-source CFD code SU2-NEMO * (NonEquilibrium MOdels). The software has been developed for the purpose of simulating chemically-reactive and nonequilibrium flows and has been extensively validated [18]. The closure of the governing equations for the system of interest is achieved by means of coupling with appropriate thermochemistry models. In this regard, the CFD solver is linked to the external library Mutation++ library† [19] (Multicomponent Thermodynamic And Transport properties for IONized gases in C++), that provides efficient algorithms for the computation of thermodynamic, transport (viscosity, thermal conductivity and diffusion) and chemical kinetic gas properties for a given state of the mixture. The library has been designed for robustness over a wide range of temperatures and its accuracy in dealing with multi-temperature models. The library has been extensively validated as a software on its own [19] and some validation work has been carried out for the coupling with the CFD solver [11]. The approach adopted for numerical discretization is a finite-volume edge-based formulation used with the AUSM scheme [28] (Advection Upstream Splitting Method) together with MUSCL (Monotonic Upstream-centered Scheme for Conservation Laws) and the Venkatakrishnan-Wang limiter. A dual time-stepping approach with a second-order backward-difference discretization is adopted to address unsteadiness.

IV. Flow patterns over a double-wedge

The flow over a double-wedge geometry is characterized by two compression corners. When the supersonic freestream encounters the first wedge's leading edge, an oblique shock forms, deflecting the streamlines according to the wedge's angle. Likewise, another oblique shock is generated at the compression corner between the two wedges. Depending on the freestream flow conditions, the lengths and angles of the two wedges, and the characteristics of the gas, the flow patterns arising from the interference of these two oblique shocks will result in different shock interaction mechanisms.

Figure 1 shows the schematic of two different generic inviscid shock interactions: type VI and type V [13]. In the type VI interaction, the flow is purely supersonic and the oblique shock waves originating at the two corners, the leading shock LS and the corner shock CS, directly intersect at point P. As a result, a contact discontinuity CD occurs, which distinguishes the flow that has travelled through both shocks, LS and CS, from the flow that has only passed through the bow shock, BS. An expansion wave EW is emitted from the oblique shock intersection and reflected on the surface of

*https://github.com/su2code/SU2

†https://github.com/mutationpp/Mutationpp

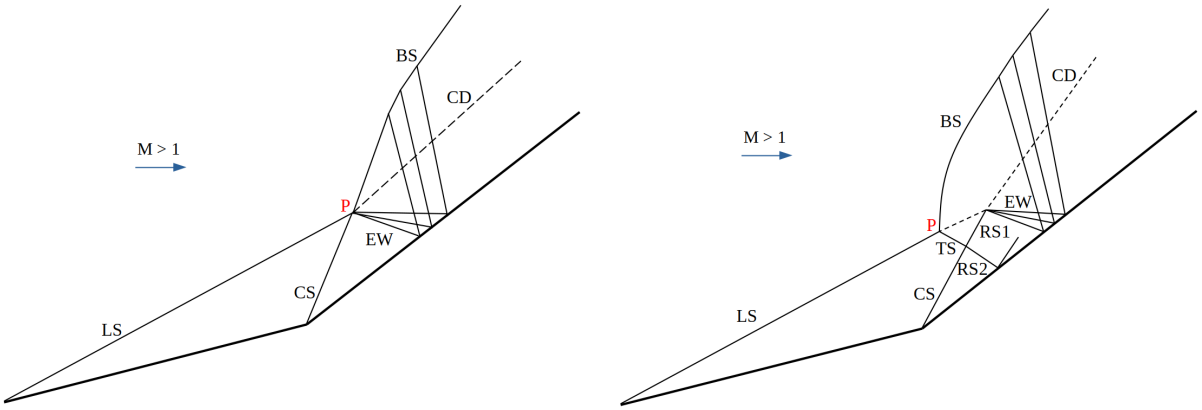

(a) Type VI. **(b) Type V.**

Fig. 1 Shock-shock interaction patterns.

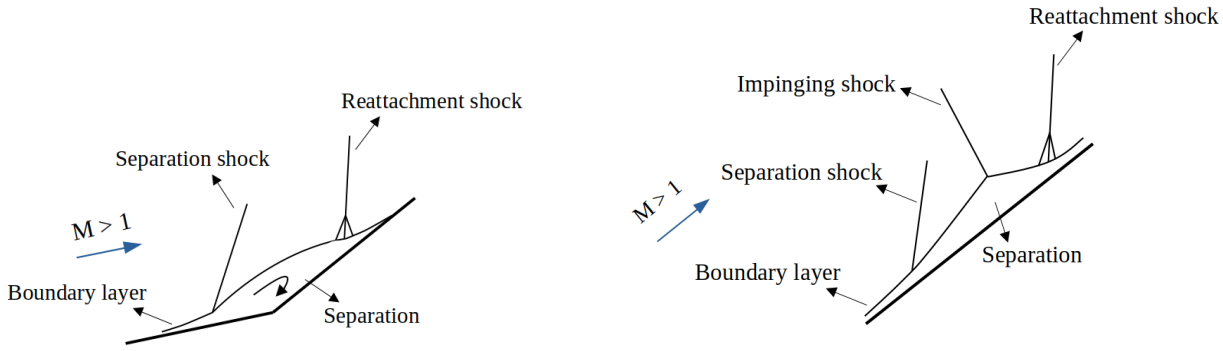

(a) Compression corner recirculation bubble and shock wave system.

(b) Shock wave system in the case of boundary layer separation due to shock impingement on the surface.

Fig. 2 Shock-boundary layer interaction patterns.

the second wedge. The type V interaction is characterized by one triple point P, where the leading shock LS, the bow shock BS and transmitted shock TS intersect. The latter shock interacts with the oblique shock CS generated by the corner between the two wedges, in a shock reflection structure [29]: shock TS reflects as shock RS1 and shock CS reflects as shock RS2, which in turn reflects on the surface of the second wedge. The reflection of the two shocks from opposite families, CS and TS, is one of the key features in the type V interaction. Furthermore, a contact discontinuity CD is generated at the triple point P and, as a consequence of the reflection of shock RS1 in the contact discontinuity, an expansion wave EW forms and reflects on the surface of the second wedge.

When viscous effects are present, shock waves and contact discontinuities are no longer discontinuities, but take the form of high-gradient regions, which may have an substantial impact on how the flow develops. The presence of a nonequilibrium thermal boundary layer generates a gradient of temperature near the wall, resulting in surface aerodynamic heating. Moreover, the inclusion of viscous effects in the simulation of this type of flows generates additional flow features such as boundary layers, recirculation zones, vortices, etc. The interaction between the different shock waves and the flow features arising from viscous effects leads to increasingly complex flow physics that can result in localized severe peaks of pressure and heat flux along the surface. As the boundary layer develops along the surface of the fore wedge, the adverse pressure gradient resulting from the presence of the second wedge interacts with the boundary layer, potentially causing flow separation ahead of the corner (schematic in Fig. 2a). The flow then reattaches at a certain location on the aft wedge surface and a recirculation bubble is formed below the slip line. This bubble acts as a new wedge, since the supersonic flow over the slip line is forced to adopt the new velocity direction. As a result, the leading shock LS generated at the beginning of the first wedge intersects with the separation shock caused by

Table 1 Simulation parameters.

M_∞	p_∞ [Pa]	T_∞ [K]	T_{wall} [K]	Mole fractions
7, 9, 11	10	160	300	CO_2: 0.97 N_2: 0.03

the recirculation bubble. Figure 2a shows a conceptual sketch of the key features expected. Besides the presence of a separation/detachment shock wave, reattachment of the boundary layer leads to a series of compression waves that may coalesce and form another shock. At the reattachment point, the boundary layer becomes very thin and the pressure is high, resulting in a region of very high aerodynamic heating [30]. Additionally, the shock wave interaction over the double-wedge may result in shock impingement on the surface, as illustrated in Fig. 2b. Given the presence of viscous effects, the impinging shock interacts with the boundary layer (SBLI), introducing an adverse gradient of pressure. If this interaction is strong enough, it may cause the boundary layer to separate in the vicinity of the impingement point, generating additional separation and reattachment shocks.

V. Effect of Mach number on shock interaction mechanisms

A. Geometry, flow conditions and grid convergence

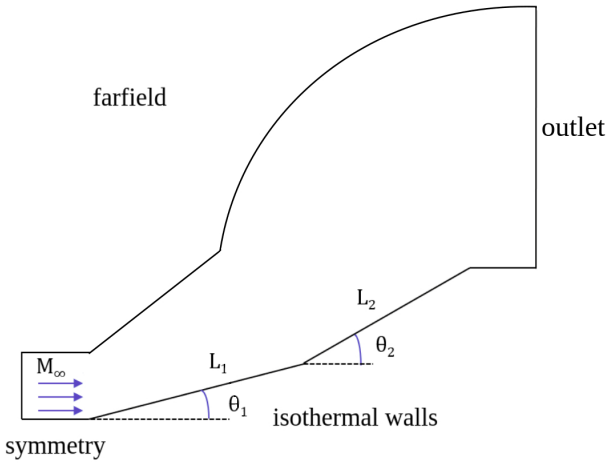

Fig. 3 Double-wedge geometry, computational domain and boundary conditions.

The double-wedge geometry considered in this study is illustrated in Fig. 3. Four different configurations are considered with a fixed fore angle of 15°and aft angles of 45°and 55°. For all cases, $L_1 = L_2 = 0.2$ m. The two wedge surfaces and the expansion surface downstream of the expansion corner are assumed to be isothermal walls. For the leftmost horizontal segment a symmetry boundary condition is applied. An outlet boundary condition is chosen for the exit and farfield is considered for the remaining boundaries. Numerical simulations are performed for a flow of CO_2:97%, N_2:3% referring to the atmosphere of Mars. Simulation parameters, presented in Table 1, are chosen so that the freestream conditions are in the laminar continuum regime and values of pressure and temperature that can be found in the Martian atmosphere. The freestream flow is assumed to be in thermal equilibrium.

The flow over a double-wedge geometry typically generates a complex interaction between different flow features, including shock waves, boundary layer, shear layers, etc. These features are very localized, highly directional and characterized by sharp gradients, but they frequently split zones of essentially uniform flow. In the attempt to minimize computational costs while accurately capturing the shock interaction mechanisms, automatic anisotropic mesh adaptation is used to generate meshes. Anisotropic meshes allow for a clustering of nodes and stretching of the elements in such a way that no significant increase in number of nodes is necessary to improve the accuracy of the solution. Because all flow features translate to Mach number gradient and are thus detected by the adaptation process, the Mach number is chosen as a variable to compute the metric field used for adaptation.

Grid convergence is assessed qualitatively, on the basis of the establishment of a given shock interaction pattern,

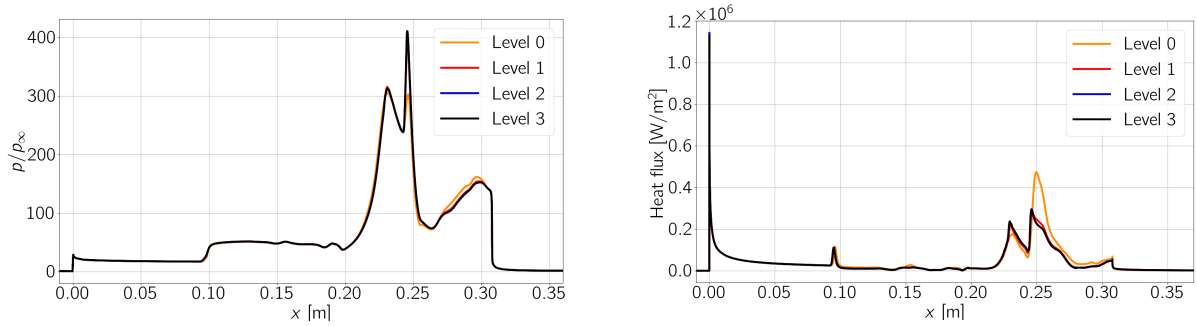

(a) Normalized surface pressure. **(b) Surface heat flux.**

Fig. 4 Grid convergence study for the case of the 15-°-55°double-wedge with $M_\infty = 11$.

and quantitatively, by comparing normalized wall surface pressure and wall surface heat flux. Previous studies on shock interaction patterns [8] additionally analysed temperature profiles normal to the wall to assess grid convergence, however the wall surface heat flux revealed to be the last quantity to converge. A grid convergence study was performed for all test-cases, but for simplicity, only the case of the 15°-55°double-wedge with $M_\infty = 11$ is showcased. Quantitative comparisons for the different levels of adaptation are shown in Fig. 4. Results obtained for levels 2 and 3 are essentially superimposed for both surface normalized pressure and heat flux, proving grid convergence.

B. 15°-45°double-wedge

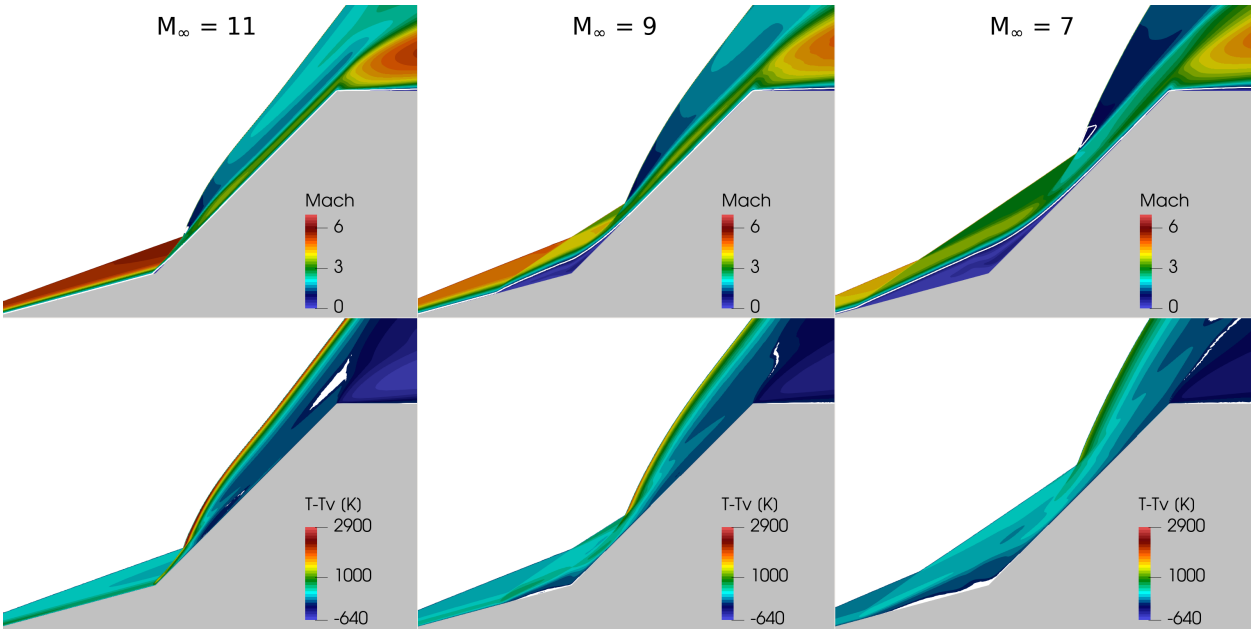

Fig. 5 Contours of Mach number (top) and difference between translational and vibrational temperatures (bottom) for a CO_2-N_2 flow over the 15°-45°double-wedge with $M_\infty = 11$, $M_\infty = 9$ and $M_\infty = 7$. White regions in the bottom row represent thermal equilibrium.

1. Patterns of interaction

Figure 5 shows contours of Mach number and difference between translational and vibrational temperatures (which measures thermal nonequilibrium) for the flow over the 15°-45°double-wedge for decreasing freestream Mach number:

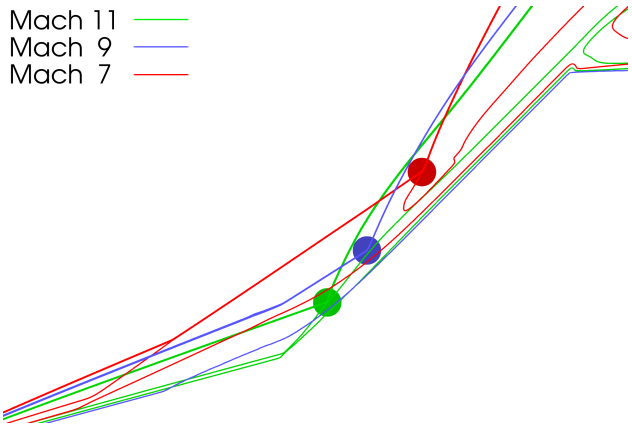

Fig. 6 Comparison of Mach number contour lines for different values of freestream Mach (7, 9, 11) for the 15°-45°geometry.

11, 9, 7. All three cases display a type VI interaction, characterized by the direct interaction of oblique shocks that results in a combined shock BS (typically bow shock), expansion wave EW and contact discontinuity CD (inviscid schematic provided in Fig. 1a).

It is well known from inviscid gas dynamics that, in a flow over a wedge, increasing the freestream Mach number causes the oblique attached shock wave, or the detached bow shock, to move closer to the body. For the case of an attached shock, the smaller standoff distance is also associated to lower shock angles. In Fig. 6, Mach contour lines for the three cases are plotted over each other. It is seen that for the leading shock LS, which occurs only due to the presence of the first wedge, the shock standoff distance and angle continuously increase with decreasing Mach number, following the expected trend. For the bow shock BS, this is only verified further downstream, where there is less influence of the main shock interaction near the compression corner. The triple-point P also travels further away from the wall as Mach number decreases. All three cases result in a type VI interaction pattern (see Fig. 1a). However, due to a much smaller size of the recirculation bubble in the corner between the two wedges, the case of $M_\infty = 11$ gives rise to a different system of shock waves near this region. Since the higher value of freestream Mach number leads to a weaker corner shock CS when compared to the cases of $M_\infty = 9$ and $M_\infty = 7$, the region of flow recirculation resulting from the adverse pressure gradient is also significantly smaller. For that reason, the flow compression associated to detachment and subsequent reattachment of the boundary layer coalesce into a single shock, which in turn interacts directly with the leading shock LS at point P. As the freestream Mach increases, i.e. $M_\infty = 9$ and $M_\infty = 7$, the stronger corner shock CS causes the boundary layer to separate further upstream leading to a larger region of separated flow. Accordingly, the detachment shock, generated at the point of separation, occurs significantly further upstream of the corner and interacts with the leading shock LS in a secondary type VI interaction. For these two cases, the main type VI interaction pattern occurring at point P is instead a consequence of the interference between the reattachment shock and the combined oblique shock resulting from the secondary type VI interaction. Furthermore, it is seen that the more upstream is the location of the separation point, the larger is the angle of the detachment shock and and the further downstream is the location of the main interaction (triple-point P), see Fig. 6. The sonic line in Fig. 5 indicates that, besides the boundary layer, subsonic flow regions are found behind the bow shock for $M_\infty = 11$ and $M_\infty = 7$. When a type VI interaction results in subsonic pockets behind the bow shock, it is named as supercritical type VI interaction [4]. A very small subsonic pocket is seen just downstream the triple-point P for $M_\infty = 11$, whereas no subsonic flow exists behind the bow shock BS for $M_\infty = 9$. Even though it is expected that a lower freestream Mach number $M_\infty = 9$ would lead to lower post-shock velocities, and eventually a larger subsonic region than for $M_\infty = 11$, this is not the case. As mentioned before, the very small region of flow separation in the case of $M_\infty = 11$ generates one single shock resulting from detachment and subsequent reattachment of the boundary layer. Because the these two stages of flow compression are combined into one shock, the associated shock strength and angle are larger than for the detachment shock in the case of $M_\infty = 9$, that is generated only due to boundary layer detachment. As a consequence, there is a larger curvature of the bow shock BS near the triple-point P for $M_\infty = 11$, leading to the lower and subsonic velocities. From $M_\infty = 9$ to $M_\infty = 7$, the angle of the detachment shock DS increases again and the expected trend is obtained, with a subsonic pocket being generated for the lower freestream Mach $M_\infty = 7$.

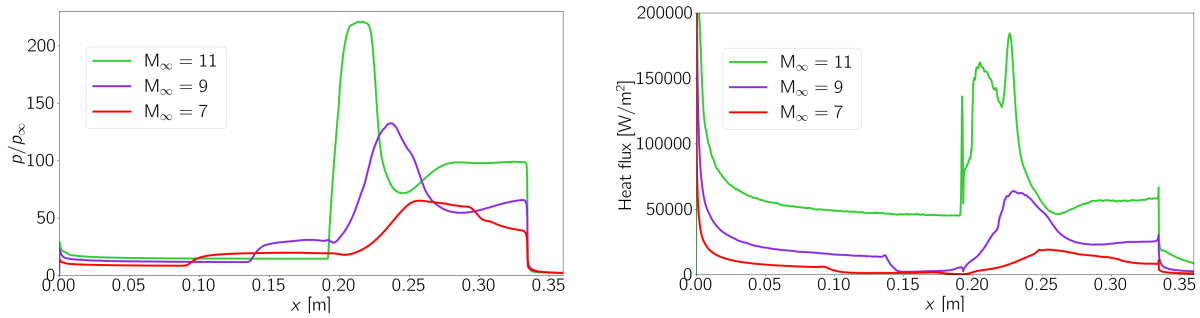

(a) Normalized pressure. **(b) Heat flux.**

Fig. 7 Comparison of surface quantities distribution for different freestream Mach numbers for the 15°-45°geometry.

2. Nonequilibrium effects

As previously mentioned in Sec. V.B.1, higher Mach numbers tend to reduce the oblique shock angle and the bow shock standoff distance. When real effects play a significant role, this tendency is further emphasized: higher freestream Mach numbers lead to increasing nonequilibrium behind the shock, i.e., a larger amount of internal energy is transferred to the vibrational modes and dissociation reactions are more likely to occur, which overall contributes to increasing post-shock density and smaller shock standoff distance [8].

When it comes to chemical reactions, the flow revealed to be chemically frozen for all the three cases since temperatures are not high enough to trigger dissociation. However, as seen in the bottom row of Fig. 5, most part of the flowfield is in thermal nonequilibrium. From the theory of gas dynamics, it is known that stronger thermal nonequilibrium occurs for higher Mach flows. Indeed, the largest difference between translational and vibrational temperatures is obtained for $M_\infty = 11$, in the flow region just behind the bow shock. On the other hand, equilibrium tends to be reached in regions of low velocity, where the flow times scales become much larger than the times associated to vibrational relaxation. This occurs inside the separated flow region, where subsonic velocities are reached. Since larger separated regions are obtained for decreasing Mach number, it is also seen that larger portions of the domain are in thermal equilibrium near the compression corner. Towards the expansion corner, the opposite trend is observed. As Mach number decreases, which in turn leads to lower post-shock temperatures and post-shock velocities, one could expect that thermal equilibrium is more likely to be reached. However, the higher pressures resulting from higher freestream Mach number contribute to accelerating the process of internal energy transfer between translational and vibrational modes, which leads to decreasing regions of thermal equilibrium downstream of the bow shock with decreasing Mach number.

3. Surface quantities

Figure 7 shows the distribution of surface quantities at the wall, namely normalized pressure and heat flux. As expected, lower values of freestream Mach number result in overall lower distributions of pressure and heat flux at the surface. The plots show the same qualitative distribution for $M_\infty = 9$ and $M_\infty = 7$, which confirms that an identical pattern of shock interaction is obtained for these two cases. An initial increase/decrease in pressure/heat flux is seen at approximately $x = 0.09$ m and $x = 0.135$ m, for $M_\infty = 9$ and $M_\infty = 7$ respectively, corresponding to the point of boundary layer separation. Further downstream, the peaks of pressure seen at $x = 0.23$ m and $x = 0.255$ m are associated with the reattachment of the boundary layer. The parametric study shows that, for lower freestream Mach numbers, the larger separated regions reattach more gradually, which is indicated by the significantly wider peaks of pressure and heat flux. For the $M_\infty = 11$ case, it is now clear from the normalized surface pressure plot that flow detachment and reattachment converge into one single stage of compression associated to one single shock, since this quantity only increases once, with a peak at approximately $x = 0.215$ m. The heat flux distribution around the compression corner, on the other hand, is slightly more complex. The first spike of heat flux occurs at the point of boundary layer separation. The separated boundary layer is usually associated with decreasing heat flux. However, by visualizing contours of translational temperature and the sonic line with a close-up near the compression corner, at the left side of Fig. 8, it can be seen that the detachment shock compresses the flow against the wall at the point of

separation, $x = 0.191$ m, which causes the wall heat flux to spike at this location. Just downstream, where the boundary layer detaches from the wall, the heat flux decreases, with a downward spike at the location of the corner (see Fig. 7). It then starts gradually increasing until reaching the wide peak of approximately 162,000 W/m^2 at $x = 0.205$ m, resulting from the gradual reattachment of the boundary layer (indicated by the sonic line that gradually gets closer to the wall, at the left of Fig. 8). The following decrease occurs due to the presence of the expansion wave EW, that causes the flow to cool down. However, instead of undergoing a gradual decrease of heat flux up to the expansion corner, the largest peak of heat flux of 184,500 W/m^2 occurs at approximately $x = 0.227$ m. By looking at right of Fig. 8, it can be concluded that this is mainly due to the contribution of vibrational temperature, which reaches a local maximum in this region (yellow contour), simply as a result of the internal energy transfer process.

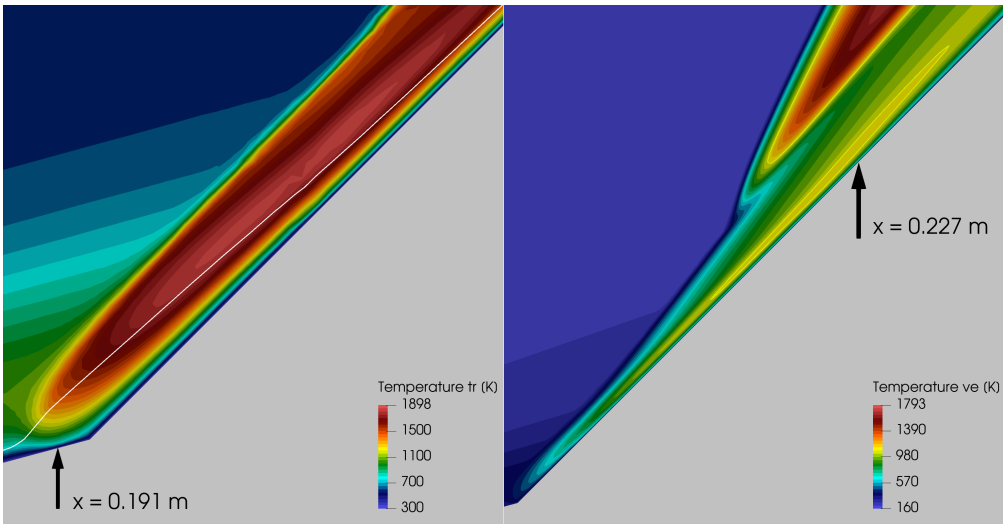

Fig. 8 Compression corner detailed views of the 15°-45°double-wegde with $M_\infty = 11$. Left - translational tempeature with sonic line, right - vibrational temperature.

C. 15°-55°double-wedge

1. Patterns of interaction

For the 15°-55°double-wedge, all three values of freestream Mach number result in a type V interaction pattern (Fig. 1b). The $M_\infty = 7$ did not reach a steady state, therefore the solution obtained with the steady state solver was provided as a first guess to resolve the unsteady shock interaction process with time-accurate simulations. Figure 9 shows contours of Mach number and difference between translational and vibrational temperatures (which measures thermal nonequilibrium) for the flow over the 15°-55°double-wedge for freestream Mach numbers 11 and 9. Figure 10 shows the Mach number contours for the $M_\infty = 7$ case. In this figure, contours are shown for four different instants of time, where the first and fourth instant of time depict essentially the same shock interaction pattern, showing that the flow is periodic in time.

The type V interaction pattern is characterized by the reflection of two shocks from opposite families. For the solutions presented in this section, this reflection occurs between the reattachment shock and the transmitted shock generated at the triple-point. This reflection can be a regular reflection RR or a Mach reflection MR, where an additional normal shock connects the points of reflection. For $M_\infty = 11$ and $M_\infty = 9$, a type V interaction with RR reflection is obtained. The pattern of interaction, including the flow features resulting from the presence of viscous effects, is similar. Some of the differences between $M_\infty = 11$ and $M_\infty = 9$ follow the trends observed for the 15°-45°double-wedge. A larger recirculation bubble in the compression corner is obtained for the lower Mach number, which in turn results in a leading shock and detachment shock characterized by larger angles - see Fig. 11. Moreover, a larger subsonic region is seen behind the bow shock (see Fig. 12), that is also characterized by a larger standoff distance for the lower Mach number. The most significant differences in the mechanism of interaction are in the main region of shock interference, that is zoomed in in Fig. 12. In this region, for both cases there is shock impingement (explained in Fig. 2b) on the wall of the aft wedge. For the $M_\infty = 9$ case, the impinging shock is stronger and characterized by a larger shock angle, which

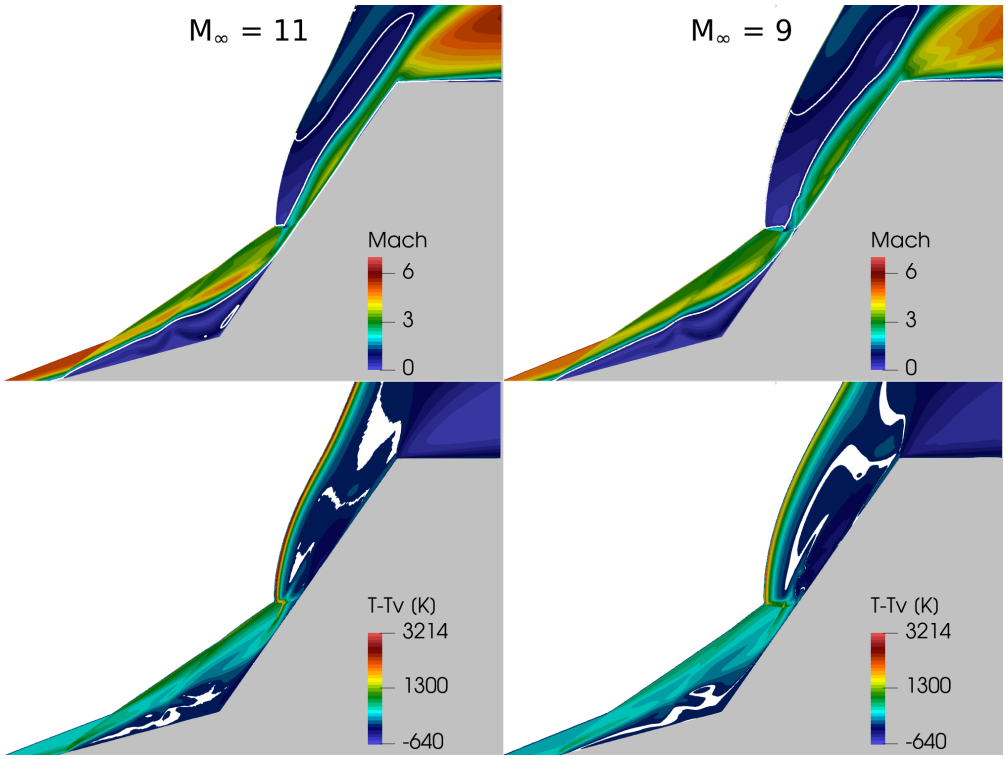

Fig. 9 Contours of Mach number (top) and difference between translational and vibrational temperatures (bottom) for a CO_2-N_2 flow over the 15°-55°double-wedge with $M_\infty = 11$ and $M_\infty = 9$. White regions in the bottom row represent thermal equilibrium.

results in a stronger SBLI. For the $M_\infty = 11$ case, the shock induced boundary layer separation is quite small and does not generate any additional shocks. For $M_\infty = 9$, the separation resulting from shock impingement is larger enough to generate additional detachment and reattachment shocks occurring upstream and downstream of the separation point, respectively. The two shocks can be clearly visualized in the pressure contours of the bottom row in Fig. 12, from the transition of light blue to green contours (detachment shock) and green to yellow contours (reattachment shock). It is concluded that a more complex shock interaction pattern, with a larger number of interacting shock waves, is obtained for the $M_\infty = 9$ case. By looking at Fig. 11, from the locations of both triple-points, it can be extrapolated that when separation from shock impingement occurs, the main region of interaction is pushed upstream. Since a larger separation due to shock impingement is obtained for $M_\infty = 9$, the triple-point is therefore located more upstream than for $M_\infty = 11$. It is relevant to notice that this trend is opposite of what was seen for the 15°-45°geometry, where there is no shock impingement on the wall.

As stated before, the $M_\infty = 7$ case results in a periodic mechanism of shock interaction. The periodicity of the flow can be seen in the matching patterns of interaction between the first and fourth instant of time in Fig. 10. Comparing to the larger values of freestream Mach number, $M_\infty = 11$ and $M_\infty = 9$, the separation bubble increases significantly. The shock angles are also much larger and the location of the triple-point is substantially further downstream, towards the expansion corner. Instead of the steady type V regular reflection pattern obtained for $M_\infty = 11$ and $M_\infty = 9$, the stronger shocks lead to an oscillating type V pattern that continuously changes between a Mach reflection and a regular reflection of the reattachment and transmitted shocks. It is relevant to notice that, for this case, very large regions of the domain result in subsonic flow. Similarly to the previous cases, subsonic velocities are found in the separated boundary layer, near the compression corner as well as location of shock impingement, and behind the bow shock. For $M_\infty = 7$, however, an additional subsonic pocket is seen behind the Mach stem, for the first, second and fourth instants of time.

Periodic mechanisms of shock interaction have been analysed before in various works [5, 7, 8, 31]. Unsteadiness in the viscous type V interaction has been explained by the strong coupling between the recirculation bubble, the impinging shock and the bow shock. As the reflected shock impinges on the surface of the aft wedge and separates the boundary layer, the resulting adverse pressure gradient travels upstream through the subsonic portion of the boundary layer, and

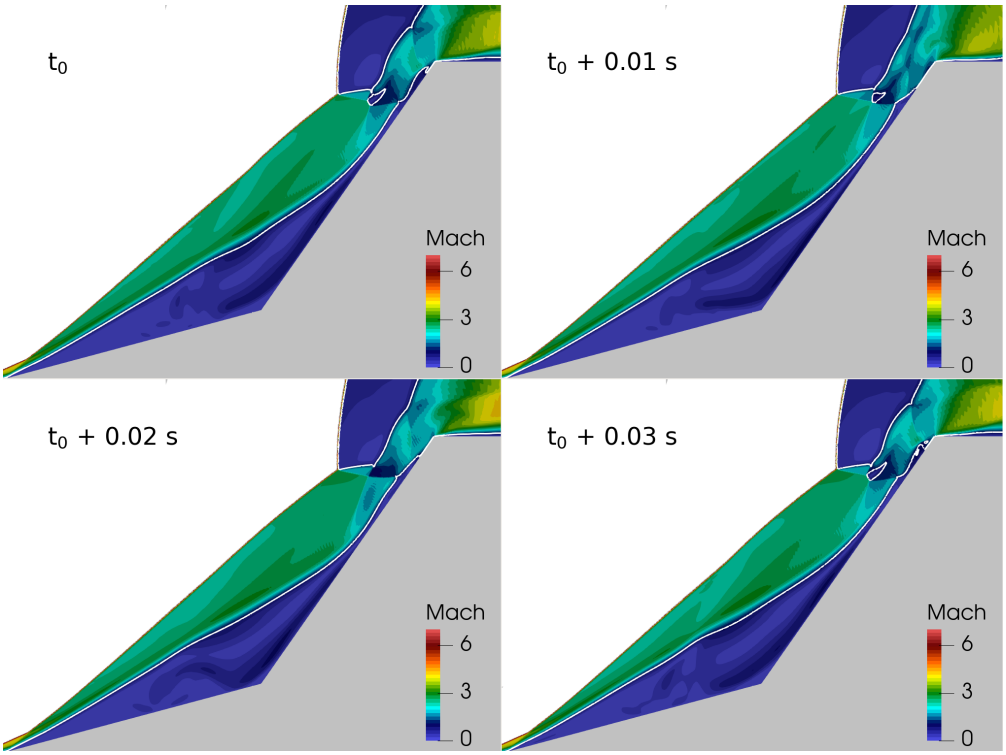

Fig. 10 Contours of Mach number for a CO_2-N_2 flow over the 15°-55°double-wedge with $M_\infty = 7$.

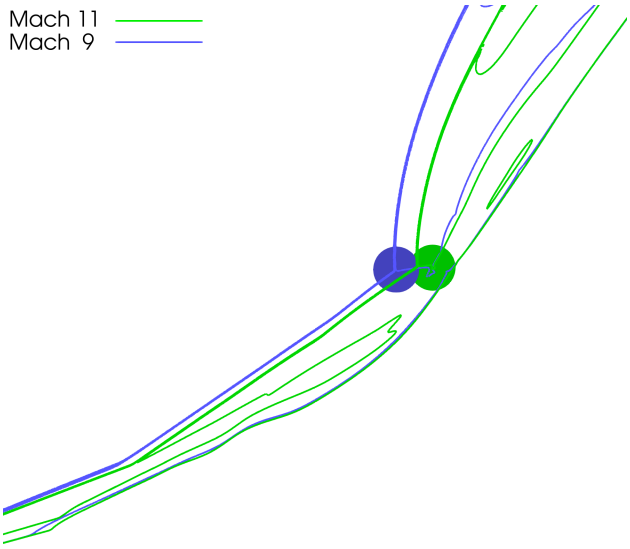

Fig. 11 Comparison of Mach number contour lines for different values of freestream Mach (9, 11) for the 15°-45°geometry.

feeds the vortex dynamics inside the recirculation bubble. As the main region of interaction travels downstream, the impinging shock becomes weaker, the vortex energy inside the separation bubble decays and the motion of the whole shock system changes direction.

When it comes to the behaviour of thermal nonequilibrium effects, shown in the bottom row of Fig. 9, no major differences are seen in the parametric study, relative to the trend seen for the 15°-45°geometry.

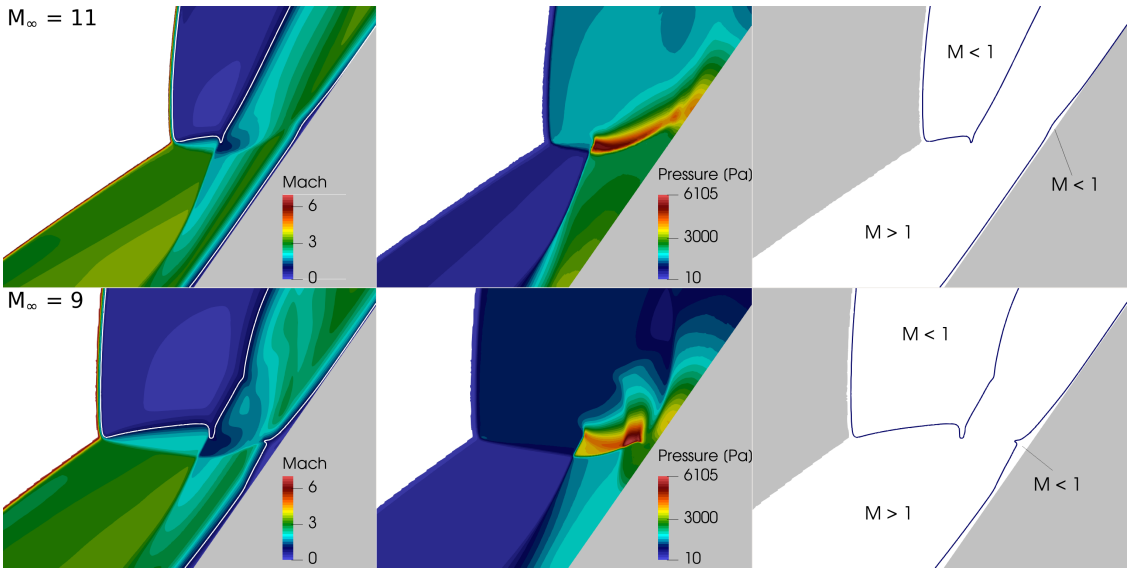

Fig. 12 Close-up in the region of main interaction: $M_\infty = 11$ (top) and $M_\infty = 9$ (bottom) for a CO_2-N_2 flow over the 15°-55°.

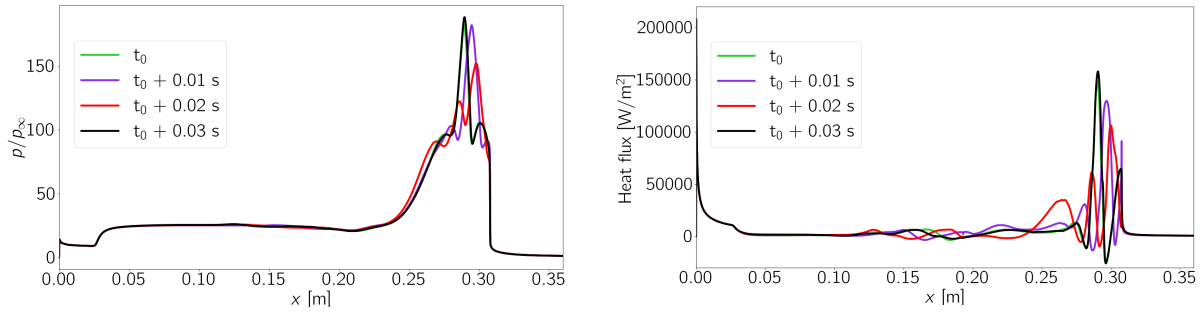

(a) Normalized pressure. **(b) Heat flux.**

Fig. 13 Instantaneous surface quantities distribution for the $M_\infty = 7$ flow over the 15°-55°geometry.

2. Surface Properties

Figure 13 shows the instantaneous distribution of surface quantities for the 15°-55°double-wedge with $M_\infty = 7$ case. The periodicity of the flow pattern is here confirmed by the matching distributions of normalized pressure and heat flux for the instants of time t_0 and $t_0 + 0.03$ s. In the normalized surface pressure plot, it can be seen that, between t_0 and $t_0 + 0.01$ s, the point of impingement travels downstream and the pressure peak intensity decreases. At $t_0 + 0.02$ s, this effect is further emphasized, and the reattachment shock already travels slightly upstream, which would correspond to the stage of decaying vortex energy (the reattachment shock is indicated by the pressure increase in the region 0.235 - 0.270 m). The heat flux distribution is slightly more difficult to analyse in the main region of interaction due to the numerous local minima and maxima associated to reattachment and separation regions. However, the fluctuations in the vicinity of the compression corner are a strong indicator of the unsteady vortex dynamics inside the recirculation bubble.

Figure 14 shows a comparison of surface properties for all 15°-55°cases, Mach 11, 9 and 7 is shown in Fig. 14. For the unsteady case, a time average is plotted. The differences in the pattern of interaction between $M_\infty = 11$ and $M_\infty = 9$ are reflected on the distribution of surface quantities. Up until the compression corner at $x = 0.193$ m, the plots are qualitatively identical. For $M_\infty = 11$, downstream of the corner, the normalized surface pressure exhibits two peaks, associated with boundary layer reattachment and shock impingement. The surface heat flux distribution follows the same behaviour, with a significant decay between the two peaks, corresponding to boundary layer reattachment in the compression corner and shock induced boundary layer separation, respectively. On the other hand, the surface pressure

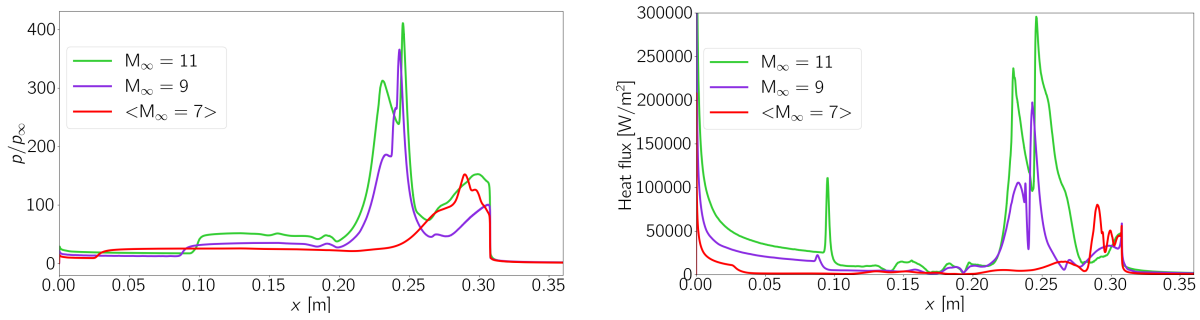

(a) Normalized pressure. **(b) Heat flux.**

Fig. 14 Comparison of surface quantities distribution for different freestream Mach numbers for the 15°-55°geometry. For $M_\infty = 7$, the time average is plotted.

of the $M_\infty = 9$ cases continuously increases from the first separation point at $x = 0.085$ m, as a result of the successive shocks: compression corner separation and detachment shocks, as well as separation and detachment shocks due to impingement. The heat flux distribution for the case $M_\infty = 9$, in Fig. 14b, is also indicative of these four shocks: 1) flow separation due to the compression corner shown by the small peak and followed by decreasing heat flux at $x = 0.088$ m, 2) subsequent reattachment peak at $x = 0.233$ m, 3) flow separation due to shock impingement indicated by the very narrow peak and subsequent decrease at $x = 0.283$ m and 4) reattachment downstream of the region of shock impingement at $x = 0.243$ m.

Similarly to the 15°-45°double-wedge, decreasing freestream Mach number leads to overall lower distributions of surface normalized pressure and heat flux. Even though the red line corresponds to a time-averaged solution, by looking at Fig. 13, we conclude that this is also the case for the instantaneous distributions. The maximum instantaneous normalized pressure is approximately 188 for $t_0 + 0.03$ s, which is 1.9 and 2.2 smaller than the largest peaks obtained for, respectively, $M_\infty = 9$ and $M_\infty = 11$. For the surface heat flux, the maximum instantaneous value is 158,000 W/m^2 for $t_0 + 0.03$ s, which is 1.25 and 1.87 smaller than maximum heating values obtained, respectively, for $M_\infty = 9$ and $M_\infty = 11$. In Fig. 14, it is also interesting to notice that the location of shock impingement travels upstream from $M_\infty = 11$ to $M_\infty = 9$, and downstream from $M_\infty = 9$ to $M_\infty = 7$. This is because between Mach 11 and 9 the size of the recirculation bubble and shock interaction pattern is quite similar, expect for the larger separation region in the location of impingement for $M_\infty = 9$, that pushes the triple-point and the region of main interaction upstream. On the other hand, from $M_\infty = 9$ to $M_\infty = 7$ the size of the recirculation bubble becomes much larger and the main region of the interaction, including shock impingement, occurs closer to the expansion corner. Furthermore, particularly in the case of the heat flux distributions, vortex dynamics in the recirculation bubble is indicated by the fluctuations of surface heating from approximately $x = 0.088$ m to $x = 0.219$ m.

VI. Conclusions

It is well known from inviscid gas dynamics that, in a flow over a single wedge, increasing the freestream Mach number causes the oblique attached shock wave, or the detached bow shock, to move closer to the body. Moreover, when real effects play a significant role, this tendency is further emphasized: higher freestream Mach numbers lead to increasing nonequilibrium behind the shock, i.e., a larger amount of internal energy is transferred to the vibrational modes and dissociation reactions are more likely to occur, which overall contributes to increasing post-shock density and smaller shock standoff distance. In the case of a flow over a double-wedge, which presents two compression corners, different shock waves interact with each other and complex non-linear changes in the flow are expected to take place when freestream conditions vary.

In this work, the effect of the freestream Mach number on hypersonic shock interaction patterns over a double-wedge is investigated for carbon-dioxide flows. The parametric study revealed that, as the Mach number decreases, the size of flow separation regions increases. This showed to have a significant impact on the system of shock waves and resulting flow pattern, since depending on the size of the bubble, additional detachment and reattachment shocks may be generated and play a role in the interaction pattern. It was therefore concluded that decreasing the freestream Mach

number has an effect on the pattern of interaction similar to the one of increasing the angle of the second wedge [8]: the recirculation bubble becomes larger leading to more complex and stronger mechanisms of interaction, characterized by larger standoff distances. Additionally, for larger aft angles, there seems to be a threshold of the Mach number below which the flow becomes unsteady. Table 2 summarizes the shock interaction patterns obtained in the parametric study.

When it comes to surface aerothermal loads and presence of thermal nonequilibrium effects, the trend seems to oppose to the one resulting from increasing the aft wedge angle. Decreasing the Mach number leads to overall lower surface heating and pressure, as well as smaller regions of thermal nonequilibrium downstream of the bow shock towards the expansion corner. It was concluded that the higher post-shock pressures obtained for the higher Mach number accelerated the process of internal energy relaxation. To complete the parametric study with respect to all the relevant parameters that are expected to greatly impact shock interaction patterns, future work will look into exploring the effects of turbulence by changing the freestream Reynolds number.

Table 2 Patterns of interaction - summary.

Geometry	$M_\infty = 11$	$M_\infty = 9$	$M_\infty = 7$
15°-45°	Type VI	Type VI - Type VI	Type VI - Type VI
15°-55°	Type V with RR reflection	Type V with RR reflection + shock impingement pattern	Unsteady oscillating Type V between MR reflection and RR reflection + shock impingement pattern

Acknowledgments

The authors wish to acknowledge the support the EPSRC funded ARCHIE-WeSt High Performance Computer (www.archie-west.ac.uk).

References

[1] Tchuen, G., Fogue, M., Burtschell, Y., Zeitoun, D., and Ben-Dor, G., "Shock-on-shock interactions over double-wedges: comparison between inviscid, viscous and nonequilibrium hypersonic flow," *Shock Waves*, edited by K. Hannemann and F. Seiler, Springer Berlin Heidelberg, Berlin, Heidelberg, 2009, pp. 1497–1502.

[2] Tchuen, G., Burtschell, Y., and Zeitoun, D. E., "Numerical study of the interaction of type IVr around a double-wedge in hypersonic flow," *Computers & Fluids*, Vol. 50, No. 1, 2011, pp. 147 – 154. doi:https://doi.org/10.1016/j.compfluid.2011.07.002.

[3] Li, J., Zhu, Y., and Luo, X., "Thermochemical Non-equilibrium Effects on Type VI-V Transition in Hypersonic Double-Wedge Flow," *29th International Symposium on Shock Waves 1*, edited by R. Bonazza and D. Ranjan, Springer International Publishing, Cham, 2015, pp. 167–172.

[4] Olejniczak, J., Wright, M., and Candler, G., "Numerical study of inviscid shock interactions on double-wedge geometries," *Journal of Fluid Mechanics*, Vol. 352, 1997, pp. 1–25. doi:10.1017/S0022112097007131.

[5] Durna, A. S., El Hajj Ali Barada, M., and Celik, B., "Shock interaction mechanisms on a double wedge at Mach 7," *Physics of Fluids*, Vol. 28, No. 9, 2016, p. 096101. doi:10.1063/1.4961571.

[6] Thirunavukkarasu, P., and Ghosh, S., *Numerical Simulation of High Temperature Effects on High Enthalpy Flow Over Double Wedge Geometry*, AIAA Scitech 2019 Forum, San Diego, CA, AIAA Paper 2019-1904 (2019). doi:10.2514/6.2019-1904.

[7] Vatansever, D., and Celik, B., "Unsteady shock interaction mechanisms of high enthalpy reacting flows over double wedges at Mach 7," *Physics of Fluids*, Vol. 33, No. 5, 2021, p. 056110. doi:10.1063/5.0050202.

[8] Garbacz, C., Morgado, F., and Fossati, M., "Effect of thermal nonequilibrium on the shock interaction mechanism for carbon dioxide mixtures on double-wedge geometries," *Physics of Fluids*, Vol. 34, No. 2, 2022, p. 026108. doi:10.1063/5.0078233.

[9] Tumuklu, O., Levin, D. A., and Austin, J. M., "Shock-shock interactions for a double wedge configuration in different gases," *53rd AIAA Aerospace Sciences Meeting*, 2015. doi:10.2514/6.2015-1520.

[10] Tumuklu, O., Levin, D. A., Gimelshein, S. F., and Austin, J. M., "Factors influencing flow steadiness in laminar boundary layer shock interactions," *AIP Conference Proceedings*, Vol. 1786, No. 1, 2016, p. 050005. doi:10.1063/1.4967555.

[11] Garbacz, C., Maier, W., Scoggins, J., Economon, T., Magin, T., Alonso, J., and Fossati, M., "Shock interactions in inviscid air and CO_2-N_2 flows in thermochemical non-equilibrium," *Shock Waves*, 2021, pp. 1–15. doi:10.1007/s00193-021-00999-8.

[12] Pezzella, G., de Rosa, D., and Donelli, R., "Computational Analysis of Shock Wave Boundary Layer Interactions in Non-equilibrium Hypersonic Flow," 20th AIAA International Space Planes and Hypersonic Systems and Technologies Conference, AIAA Paper 2015-3578 (2015). doi:10.2514/6.2015-3578.

[13] Edney, B., "Anomalous Heat Transfer and Pressure Distributions on Blunt Bodies at Hypersonic Speeds in the Presence of an Impinging Shock," 1968. Report 115. Flygtekniska Foroksanstalten, Stockholm: The Aeronautical Research Institute of Sweden.

[14] Durna, A., and Celik, B., "Time-periodic shock interaction mechanisms over double wedges at Mach 7," *Shock Waves*, Vol. 29, 2019. doi:10.1007/s00193-018-0864-7.

[15] Durna, A. S., and Celik, B., "Effects of Double-Wedge Aft Angle on Hypersonic Laminar Flows," *AIAA Journal*, Vol. 58, No. 4, 2020, pp. 1689–1703. doi:10.2514/1.J058754.

[16] Windisch, C., Reinartz, B. U., and Müller, S., "Investigation of Unsteady Edney Type IV and VII Shock-Shock Interactions," *AIAA Journal*, Vol. 54, No. 6, 2016, pp. 1846–1861. doi:10.2514/1.J054298.

[17] Park, C., "Review of chemical-kinetic problems of future NASA missions. I - Earth entries," *Journal of Thermophysics and Heat Transfer*, Vol. 7, No. 3, 1993, pp. 385–398. doi:10.2514/3.431.

[18] Economon, T. D., Palacios, F., Copeland, S. R., Lukaczyk, T. W., and Alonso, J. J., "SU2: An Open-Source Suite for Multiphysics Simulation and Design," *AIAA Journal*, Vol. 54, No. 3, 2016, pp. 828–846. doi:10.2514/1.J053813.

[19] Scoggins, J. B., Leroy, V., Bellas-Chatzigeorgis, G., Dias, B., and Magin, T. E., "Mutation++: MUlticomponent Thermodynamic And Transport properties for IONized gases in C++," *SoftwareX*, Vol. 12, 2020, p. 100575. doi:https://doi.org/10.1016/j.softx.2020.100575.

[20] Gnoffo, P., Gupta, R., and Shinn, J., "Conservation equations and physical models for hypersonic air flows in thermal and chemical nonequilibrium," NASA Technical Paper 2867, 1989, p.158.

[21] Park, C., Howe, J. T., Jaffe, R. L., and Candler, G. V., "Review of chemical-kinetic problems of future NASA missions, II: Mars entries," *Journal of Thermophysics and Heat Transfer*, Vol. 8, No. 1, 1994, pp. 9–23. doi:10.2514/3.496.

[22] Liao, D., Liu, S., Huang, J., Jian, H., Xie, A., and Wang, Z., "Measurement and numerical simulation of shock standoff distances over hypersonic spheres in CO_2 in a ballistic range," *Shock Waves*, Vol. 30, 2020, p. 131–138. doi:10.1007/s00193-019-00923-1.

[23] Armenise, I., Reynier, P., and Kustova, E., "Advanced Models for Vibrational and Chemical Kinetics Applied to Mars Entry Aerothermodynamics," *Journal of Thermophysics and Heat Transfer*, Vol. 30, No. 4, 2016, pp. 705–720. doi:10.2514/1.T4708.

[24] Camac, M., "CO_2 Relaxation Processes in Shock Waves," *Fundamental Phenomena in Hypersonic Flow*, Cornell U.P., Ithaca, N.Y. 1966, pp. 195–215.

[25] Landau, L., and Teller, E., "Systematics of Vibrational Relaxation," *Physik Zeitschrift der Sowjetunion*, Vol. 10, 1936, pp. 34–38.

[26] Millikan, R. C., and White, D. R., "Systematics of Vibrational Relaxation," *The Journal of Chemical Physics*, Vol. 39, No. 12, 1963, pp. 3209–3213. doi:10.1063/1.1734182.

[27] Park, C., "Assessment of two-temperature kinetic model for ionizing air," *Journal of Thermophysics and Heat Transfer*, Vol. 3, No. 3, 1989, pp. 233–244. doi:10.2514/3.28771.

[28] Liou, M.-S., and Steffen, C. J., "A New Flux Splitting Scheme," *Journal of Computational Physics*, Vol. 107, No. 1, 1993, pp. 23–39.

[29] Xiong, W., Li, J., Zhu, Y., and Luo, X., "RR–MR transition of a Type V shock interaction in inviscid double-wedge flow with high-temperature gas effects," *Shock Waves*, Vol. 28, 2018, pp. 751–763. doi:10.1007/s00193-017-0770-4.

[30] Running, C. L., Juliano, T. J., Jewell, J. S., Borg, M. P., and Kimmel, R. L., "Hypersonic shock-wave/boundary-layer interactions on a cone/flare," *Experimental Thermal and Fluid Science*, Vol. 109, 2019, p. 109911. 10.1016/j.expthermflusci.2019.109911.

[31] Kumar, G., and De, A., "Role of corner flow separation in unsteady dynamics of hypersonic flow over a double wedge geometry," *Physics of Fluids*, Vol. 33, No. 3, 2021, p. 036109. 10.1063/5.0040514.